CHEMISTRY OF MATERIALS

Article

Shielded Silver Nanorods for Bioapplications

Xiaolu Zhuo, Malou Henriksen-Lacey, Dorleta Jimenez de Aberasturi, Ana Sánchez-Iglesias, and Luis M. Liz-Marzán*

Cite This: *Chem. Mater.* 2020, 32, 5879−5889

Read Online

ACCESS | Metrics & More | Article Recommendations | Supporting Information

ABSTRACT: Silver is arguably the best plasmonic material in terms of optical performance. However, wide application of Ag and Ag-containing nanoparticles is usually hindered by two major drawbacks, namely, chemical degradation and cytotoxicity. We report herein a synthetic method for highly monodisperse polymer-coated Ag nanorods, which are thereby protected against external stimuli (oxidation, light, heat) and are noncytotoxic to various cell lines. The monodispersity of Ag nanorods endows them with narrow plasmon bands, which are tunable into the near-infrared biological transparency window, thus facilitating application in bioanalytical and therapeutic techniques. We demonstrate intracellular surface-enhanced Raman scattering (SERS) imaging using Ag nanorods encoded with five different Raman reporter molecules. Encoded Ag nanorods display long-term stability in terms of size, shape, optical response, and SERS signal. Our results help eliminate concerns of instability and cytotoxicity in the application of Ag-containing nanoparticles with enhanced optical response, toward the development of bioapplications.
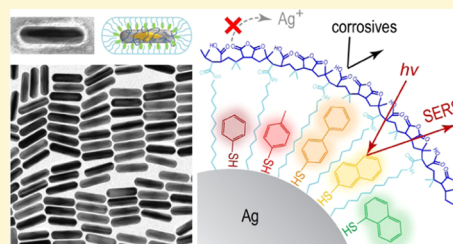
INTRODUCTION

Silver nanoparticles (Ag NPs) have received much attention in plasmonics because of their ability to support strong localized surface plasmon resonances (LSPRs) over the entire visible to near-infrared (NIR) spectral region.[1,2] A number of wet-chemistry synthetic methods have been established, which provide access to a wide variety of morphologies and particle sizes.[3−6] Owing to the unique dielectric features of Ag, such NPs display outstanding optical properties at visible−NIR frequencies, such as low ohmic losses,[7] strong local field enhancement,[8,9] and high sensitivity toward dielectric changes in the surrounding environment,[10,11] as compared to other plasmonic nanomaterials (e.g., gold, aluminum, copper). In particular, numerous studies have shown that Ag and bimetallic gold@silver (Au@Ag) NPs exhibit superior performance as sensing and imaging tools in surface-enhanced Raman scattering (SERS).[9,12] There is thus widespread agreement regarding the suitability of Ag NPs for the development of optical sensors, photocatalysts, plasmonic nanocircuits, antibacterial products, and quantum plasmonic systems.[1] However, further use, especially regarding bioapplications *in vitro*, is hindered by poor structural stability and high cytotoxicity, both of which result from Ag NP degradation.

Degradation of Ag NPs, typically including oxidation and sulfidation, may easily occur at room temperature, leading to significant spectral shifts and/or broadening of the LSPR band. The degradation rate is sensitive to storage conditions, including temperature, light exposure, surface capping, and solvent chemistry.[13] Thus, for most commercially available Ag NPs, storage in the fridge under darkness is recommended. Commonly used capping agents for Ag NPs, such as citrate,

poly(vinylpyrrolidone) (PVP), benzyldimethyl-hexadecylammonium chloride (BDAC), cetyltrimethylammonium chloride (CTAC), cetyltrimethylammonium bromide (CTAB), and thiolated poly(ethylene glycol) (PEG), are all known to protect Ag NPs from aggregation and dissolution, but such a protection fails when the NPs are exposed to air, sulfur, and other oxidizing species. As a result, the long-term storage of Ag NPs and their application in complex (biological) environments are challenging and Ag NPs are rarely used in cell culture assays. On one hand, the spontaneous dissolution of Ag NPs produces Ag^+ ions and other soluble complexes, which are toxic to most bacteria, fungi, and some cell types.[13,14] On the other hand, living cells produce reactive oxygen species (ROS, such as H_2O_2, singlet oxygen, superoxide anion, hydroperoxyl radical) and sulfides (H_2S, polysulfides), as byproducts of their cellular metabolism.[15,16] Depending on the status of the cells, the intracellular concentration of H_2O_2 is estimated to be 1−700 nM,[17] whereas the H_2S concentration can reach the micromolar level,[16] readily inducing oxidation and sulfidation of Ag NPs, respectively.

A promising approach to overcome this limitation comprises the use of protective layers, usually made of metal oxides, polymers, or biomolecules. A number of prior works have reported successful syntheses of Ag@silica,[18−20] Ag@titania,[21]

and a wide variety of Ag@polymer NPs,[22−25] most of which are based on Ag nanospheres.[26] There are however few examples where the stability and cytotoxicity of coated Ag NPs are analyzed in detail, even less focusing on anisotropic Ag NPs.[20,22,26] It has also been demonstrated that the spontaneous formation of a protein corona when Ag NPs are exposed to biofluids can effectively alter their toxicity, biological activity, and cellular internalization. Notwithstanding, NP−protein interactions are complicated in general and require further investigation.[27] In addition, direct deposition of a thin outer layer of Au atoms has been proposed as an effective method to enhance the stability of Ag nanoparticles under different corrosive environments.[28,29]

In this context, we report the synthesis of polymer-protected, monodisperse Ag nanorods (NRs), featuring high colloidal and chemical stability. We used dodecylamine-modified polyisobutylene-alt-maleic anhydride (PMA) as the protective layer, which additionally allows for the incorporation of Raman reporter (RaR) molecules toward the preparation of SERS nanotags.[30] PMA is an amphiphilic polymer, which was first used to facilitate the phase transfer of small hydrophobic NPs (metallic, semiconductor, or magnetic; size < 10 nm) into an aqueous solution,[26,31,32] and more recently, it has been extended to the encapsulation of Au NPs of different shapes, with high stability for biological applications.[33,34] RaR molecules exhibit molecular vibrations with characteristic fingerprints in SERS spectra. Compared with commercial dyes for cell imaging, SERS nanotags feature the potential of multicolor/parallel detection due to the much narrower bandwidths of Raman molecular vibration peaks than the fluorescence profiles of dyes. In addition, SERS nanotags can provide long-term stable signals for cell imaging, with signal intensities proportional to the concentration of SERS nanotags, and minimal concerns regarding photobleaching and interfering autofluorescence suffered by cell imaging using fluorescence dyes.[35]

The synthesis of Ag NRs relies on a wet-chemistry method, using penta-twinned Au bipyramids (Au BPs) as seeds to direct anisotropic Ag overgrowth. This method has been demonstrated as a robust approach to the preparation of high-quality Ag NR colloids with tailored size and optical response.[11,36] Our motivation for using these Ag NRs is 3-fold: first, they display tunable, intense, and narrow LSPR bands in the visible−NIR region; second, they are expected to boost strong local field enhancement and thereby exhibit superior SERS performance;[9] and third, Ag NRs can become a model system to study the chemical stability and cytotoxicity of Ag@PMA NPs (size > 10 nm). We demonstrate that Ag@PMA NRs retain their morphology and LSPR response upon exposure to air, oxidizing agents, light, heat, and biofluids. Since the release of Ag+ ions is suppressed by the combination of a hydrophobic ligand and a polymer layer, Ag@PMA NRs show negligible cytotoxicity to various cell lines. Additionally, by encoding Ag NRs with different RaR molecules during the polymer coating process, we obtained highly stable, non-cytotoxic, and biocompatible nanotags for intracellular SERS imaging. We further investigated the possibility of laser-induced release of Ag+ ions and cell death from photothermal effects during SERS measurements.

■ RESULTS AND DISCUSSION

Synthesis of Ag@PMA NRs. The various steps involved in the preparation of Ag@PMA NRs are schematically illustrated

in Figure 1a. Au BPs serve as seeding templates to direct Ag overgrowth along the longitudinal direction, resulting in rod-
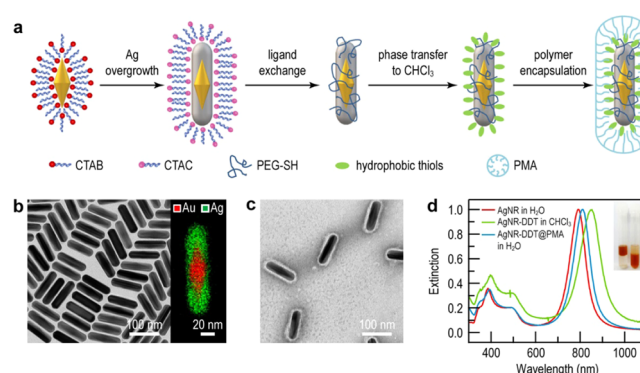

Figure 1. (a) Schematic illustration of the preparation of Ag@PMA NRs. (b) Representative transmission electron microscopy (TEM) image of cytotoxic-surfactant (CTAC)-capped Ag NRs with an average diameter of 30 ± 2 nm and an average length of 115 ± 4 nm. The inset shows the elemental mapping of one Ag NR (red, Au; green, Ag). (c) TEM image of Ag@PMA NRs, which were negatively stained with uranyl acetate. (d) Normalized extinction spectra of Ag NR prior to ligand exchange (red), after dodecanethiol (DDT) adsorption and phase transfer into CHCl₃ (AgNR-DDT, green), and after PMA encapsulation and redispersion in water (AgNR-DDT@PMA, blue). Shown in the inset is a photograph of Ag NRs in water (left) and in chloroform (right).

shaped Ag NPs (Figure 1b). The growth of nanorods is favored because of the preferential formation of {100} facets, as previously reported.[37] An important improvement of our method, compared to previous reports,[11,36] is the use of thermally treated penta-twinned Au seeds to prepare highly pure Au BPs in a single seed-mediated growth step,[38] which is then followed by Ag overgrowth to directly obtain highly pure Ag NRs in high yield, with no need for postsynthesis purification. The improved method is therefore time-efficient and more practical for large-scale production. In agreement with previous reports, the diameter of the final Ag NRs is determined by the waist diameter of the Au BP seed, whereas their length can be adjusted to basically any value greater than the length of the seed. The resulting Ag NRs exhibit at least two LSPR bands: a dipolar transverse mode centered around 400 nm and a dipolar longitudinal mode on the long-wavelength range. Multipolar modes (quadrupolar, octupolar, etc.) may additionally appear in between both dipolar modes for NRs with a high aspect ratio. The longitudinal LSPR wavelength can be tuned into the NIR biological transparency window (650−900 nm) by simply adjusting the added amount of AgNO₃ in the growth step (Figures S1 and S2). During Ag overgrowth, the longitudinal LSPR band first blue-shifts and then red-shifts due to combined effects of shape and composition, both of which have been elucidated in previous works.[11,39] Because of the high monodispersity in the Au BP seeds, the resulting Ag NRs possess outstanding uniformity in size and shape (see histograms in Figure S2), leading to narrow plasmon line widths, which are beneficial for most plasmonic applications. Moreover, it has been demonstrated that such Ag NRs with Au cores exhibit very similar near- and far-field plasmonic properties as those of pure Ag NRs with the same external dimensions.[36,40]

In the first coating step, CTAC-capped Ag NRs are protected against aggregation with a small amount of

thiolated-PEG, prior to water-to-chloroform phase transfer, in the presence of thiolated hydrophobic molecules such as dodecanethiol (DDT), which readily adsorb on Ag NRs.[41] Upon phase transfer, the amount of cytotoxic surfactant (CTAC) can be largely decreased through the formation of covalent S−Ag bonds. The same phase-transfer process can be implemented by replacing long-chain thiolated hydrophobic molecules with aromatic hydrophobic thiols, featuring strong Raman cross sections, so as to prepare SERS-encoded NPs.[34,42] Upon successful phase transfer, Ag NRs dispersed in chloroform were mixed with an appropriate amount of PMA and then subjected to rotary evaporation, during which the hydrophobic side chains (dodecylamine) of PMA get thereby interdigitated through the hydrophobic DDT chains on the Ag NR surface, so that the PMA protective layer wraps Ag NRs completely (Figure S3). As-prepared Ag@PMA NRs can be redispersed in water due to exposure of the hydrophilic backbone of PMA.[31,32] Figure 1c displays a representative transmission electron microscopy (TEM) image of Ag@PMA NRs obtained from the sample shown in Figure 1b; no obvious reshaping or degradation was observed. After negative staining, a PMA layer of ∼5 nm is observable as a bright halo surrounding each Ag@PMA NR. Changes in the extinction spectra of the same sample were monitored during the various PMA coating steps, as shown in Figure 1d. Despite minor shifts in the LSPR wavelength due to refractive index changes derived from ligand and solvent exchange, the LSPR bandwidth remained nearly unchanged, indicating a high colloidal and chemical stability of Ag NRs in every step. Similarly, the PMA coating procedure could be safely applied to other Ag NR samples of different sizes (diameters of 27 and 38 nm, and length up to 180 nm) (Figure S4). In what follows, Ag@PMA NRs are used with an LSPR wavelength centered at 800 nm, in close resonance with the NIR lasers used for both SERS imaging and photothermal effects.

Stability of Ag@PMA NRs. We analyzed in detail the colloidal and chemical stability of Ag@PMA NRs (diameter 30 ± 2 nm, average length 115 ± 4 nm) containing DDT ligands. First of all, Ag@PMA NRs can be readily dispersed in aqueous solvents, where they show high colloidal stability (Figure 1a,d). We additionally evaluated their chemical stability against well-known oxidizing species, as compared to that of CTAC-capped and PEG-capped Ag NRs, using visible−NIR spectroscopy and TEM imaging to monitor optical and morphological changes induced by oxidation. Figure 2a shows the results from the long-term optical monitoring of three Ag NR samples with different capping agents, which were stored in water at room temperature and exposed to daylight. Over a 2 month period, the longitudinal LSPR bands of both CTAC-capped and PEG-capped Ag NRs displayed an initial blue shift as the length of the Ag component is reduced, followed by a red shift, in agreement with an anisotropic oxidation process, i.e., decrease in the length of the Ag component followed by a response dominated by the Au BP cores.[36] We can also observe a gradual damping of the transverse LSPR band at 400 nm, confirming removal of the entire Ag segment from the Au BP cores, which was also confirmed by TEM (Figure S5). On the contrary, both the extinction spectrum and the morphology of Ag@PMA NRs remained unaltered under the same conditions. To verify the impact of light exposure and storage temperature, we also kept aliquots of all three Ag NR samples in the dark, at room temperature, and at 4 °C and monitored their morphological and optical changes with time (Figures S5
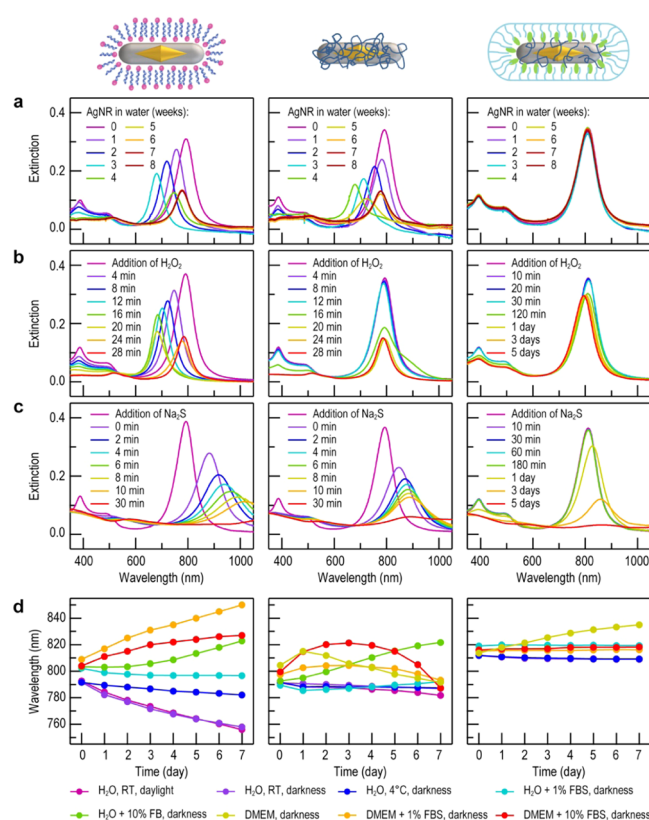

Figure 2. Comparison of the chemical stabilities of CTAC-capped Ag NRs (left), PEG-capped Ag NRs (middle), and Ag@PMA NRs (right). (a) Evolution of the extinction spectra of Ag NR colloids (6 × 10^9 NP/mL), stored in water at room temperature and under daylight, for 2 months. (b) Extinction spectra of the same samples in the presence of H$_2$O$_2$ (30 mM). (c) Extinction spectra of the same samples in the presence of Na$_2$S (1 mM). Since the extinction spectra of Ag@PMA NRs remained unchanged in the first 30 min after addition of H$_2$O$_2$ and Na$_2$S, we extended their evaluation time to 5 days. (d) Time evolution of the LSPR wavelength for all three Ag NR samples, dispersed in water and different biofluids (see labels), for 1 week.

and S6, respectively). As expected, avoiding light exposure and decreasing the storage temperature resulted in a slower Ag degradation rate for both CTAC-capped and PEG-capped Ag NRs, but changes in LSPR wavelength were still observed. For Ag@PMA NRs, these changes in storage conditions had no obvious influence on their remarkable long-term stability. We further examined the impact of light exposure using an 808 nm laser, which is a common light source to induce photothermal effects. Under continuous laser illumination at a power density of 3.0 W/cm² for 10 min, the temperature of the Ag@PMA NR colloid (∼4.5 × 10^{10} NP/mL, 200 μL) showed a gradual increase, finally reaching a plateau at 80 °C (Figure S7). Even though a much higher local temperature can be expected near the NR surface than in the bulk colloidal solution, laser illumination and the accompanying photothermal effects appear to have a minor influence on Ag@PMA NRs. As shown in Figure S7, the extinction spectrum of the heated sample remained virtually unchanged and TEM imaging with negative staining revealed no changes in the PMA layer, before and after irradiation. These results indicate that Ag@PMA NRs are excellent candidates for photothermal therapy.

Next, we challenged the stability of Ag@PMA NRs against the addition of corrosive chemicals, as it is well known that Ag can be readily degraded by oxidation or sulfidation processes.[1] We therefore selected H_2O_2 and Na_2S as representative corrosives, which can etch Ag NPs into Ag^+ ions and Ag_2S, respectively. Again, we compared the stability of Ag@PMA with that of CTAC-capped and PEG-capped Ag NRs (Figure 2b,c). We thus added a dilute H_2O_2 solution to each Ag NR sample (2 mL, 6×10^9 NP/mL), to a final H_2O_2 concentration of 30 mM. After H_2O_2 addition, we monitored the extinction spectra at room temperature, as shown in Figure 2b. Although the spectral evolution of CTAC-capped Ag NRs looks similar to that for long-term monitoring in water, corresponding to an anisotropic oxidation process, it should be noted that the process is much faster in the presence of H_2O_2, being completed within half an hour. PEG-capped Ag NRs remained stable for ca. 12 min, suggesting a certain protective effect by the PEG layer, but fast oxidation occurred thereafter, leading to an extinction spectrum corresponding to bare Au BPs within 20 min. This process can be understood as a slower diffusion of H_2O_2 from the solvent to the particle surface, in agreement with previous reports.[18,43] On the contrary, the extinction spectrum of Ag@PMA NRs remained unchanged over 30 min, and only a minor LSPR blue shift was observed within 5 days, at an extremely slow rate of 2 nm per day. Similar measurements were carried out with 1 mM Na_2S (Figure 2c). In this case, an LSPR red shift was observed for all three samples, which is likely due to the formation of Ag_2S.[11] It should be noted, however, that the sulfidation rate for Ag@PMA NRs is significantly slower than for the other two samples. Whereas for CTAC-capped and PEG-capped Ag NRs the LSPR bands were completely damped within 30 min, the spectrum of Ag@PMA NRs remained unaltered for several hours and only flattened gradually after a few days. From the corresponding TEM images, we can confirm that the PMA layer efficiently protected Ag NRs from both oxidation and sulfidation, at least for several hours (Figure S5). The protection ability of PMA relies on its amphiphilic nature,[31,32] which creates a hydrophobic interlayer between the Ag NP surface and the hydrophilic outer medium, acting as a barrier to suppress and/or slow down the diffusion of small molecules and ions dissolved in water. As a result, the stability of protected Ag NRs is greatly enhanced.

Since our main objective is the safe use of Ag NPs in bioapplications, we also investigated the stability of Ag NRs in cell culture media, which comprises a mixture of amino acids, glucose, salts, vitamins, sugars, and different types of proteins. For a meaningful comparison, we considered three types of biofluids: an aqueous solution of proteins (fetal bovine serum, FBS), Dulbecco's modified Eagle's medium (DMEM), and DMEM containing 10% v/v FBS (typically used in cell culture experiments). To exclude other effects, all samples in different biofluids were stored in the fridge under darkness, except for daily measurements of extinction spectra. Figure 2d summarizes the longitudinal LSPR maximum wavelengths for Ag NRs dispersed in water and in different biofluids during a 1-week period. Similar to the results above, we found that the stability follows the order Ag@PMA > Ag@PEG > Ag@CTAC. The constant LSPR wavelength for Ag@PMA NRs indicates a high stability in biofluids, which might be further enhanced by the formation of a protein corona outside the PMA layer.[44]

SERS-Encoded Ag@PMA NRs. The preparation of SERS-encoded Ag@PMA NRs was based on the same synthetic method as described above but replacing DDT by thiolated RaR molecules that are soluble in chloroform. Compared to the conventional functionalization with RaR molecules, this polymer coating method does not suffer from leakage, which is prevented by the hydrophobic nature of RaR molecules and interdigitation with PMA. The PMA layer provides not only protection against Ag degradation but also high biocompatibility, thus resulting in biocompatible SERS nanotags with long-term stability. We demonstrate here functionalization with five different RaR molecules: benzenethiol (BT), 4-methylbenzenethiol (4MBT), biphenyl-4-thiol (4BPT), 1-naphthalenethiol (1NaT), and 2-naphthalenethiol (2NaT), all of which can covalently bind onto the Ag surface during phase transfer. The coverage of RaR molecules on the Ag NR surface and the subsequent SERS intensity of the resulting tags are strongly influenced by the amount of PEG initially adsorbed on the Ag NRs due to competition for binding sites. Consequently, a lower PEG density favors the adsorption of RaR molecules, but the colloidal stability may be compromised by an insufficient coverage with PEG, as shown in Figure S8. After fine-tuning of the binding competition between PEG and RaR molecules, we prepared five types of SERS-encoded Ag@PMA NRs, denoted Ag@RaR@PMA NRs in what follows, all of which displayed long-term colloidal stability and strong SERS signals with characteristic fingerprints (Figures 3 and S9). For the same particle concentration, we found that Ag@BT@PMA NRs showed the strongest SERS signal. The observed differences in
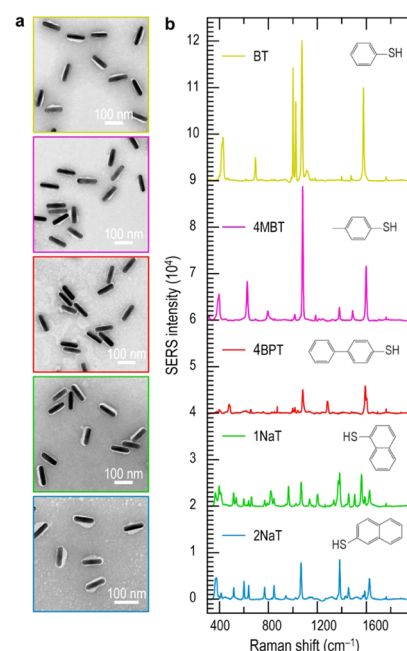

Figure 3. (a) TEM images of negatively stained Ag@RaR@PMA NRs, functionalized with five different RaR molecules. From top to bottom: benzenethiol (BT), 4-methylbenzenethiol (4MBT), biphenyl-4-thiol (4BPT), 1-naphthalenethiol (1NaT), and 2-naphthalenethiol (2NaT). (b) Corresponding SERS spectra for all five samples dispersed in water, at a particle concentration of $(1.8 \pm 0.4) \times 10^{11}$ NP/mL. All spectra were collected in the expanded scan mode, with an integration time of 10 s, using a 785 nm laser and a 10× objective (NA = 0.35) for excitation. The laser power was 3.43 mW for Ag@BT@PMA NR and 13.26 mW for the other samples. Insets show the molecular structures of the corresponding RaR molecules.

SERS intensity among the five samples can be attributed to several factors, such as the intrinsic Raman cross sections of different RaR molecules, variations of molecular density at the Ag NR surface, as well as different coupling strengths between RaR molecules and Ag NRs.

The detection limit for SERS nanotags in aqueous solution was estimated from SERS measurements at different particle concentrations, under the same experimental conditions. The results (Figure S10) show a detection limit of 4.3×10^7 NP/mL for Ag@BT@PMA NRs, which is the lowest particle concentration for which the BT SERS signal can be readily identified. Higher detection limits were determined for the other four encoded NRs, ranging from 7.0×10^8 to 1.4×10^9 NP/mL. As the focal volume of the excitation laser can be roughly calculated as a product of the laser illumination area (20 μm $\times$ 1 μm) and a field depth of 2.6 mm, the lowest number of NRs contributing to the SERS signal can be estimated to range between 3 and 72. It should be noted that these detection limits are only relevant for these specific measurement conditions; by further increasing the laser power and/or the integration time, even single-particle SERS measurements might be possible for this system. As a consequence, the different measurement conditions (water immersion objective, low-intensity laser excitation) used for SERS studies in cells lead to different detection limits, as discussed below.

For completeness, we additionally compared the SERS performance between Ag and Au NRs. To make a meaningful comparison, we applied a recently reported method to prepare highly uniform Au NRs,[45] with similar dimensions and optical responses (diameter 33 ± 3 nm, length 102 ± 7 nm, LSPR band 800 nm) to those of the Ag NRs used for the preparation of SERS nanotags. The functionalization of RaR molecules and PMA encapsulation, as well as the subsequent SERS measurements, were also carried out on Au NRs under the same conditions as those used with Ag NRs, using the same five RaR molecules. In all five cases, we recorded SERS intensities on the same order of magnitude for Au and Ag NRs (Figure S11), which seems to be in disagreement with earlier reports for similar comparisons.[9,46] Our results and discrepancies with other reports can be explained by taking into account the similar dielectric functions of Au and Ag in the NIR range, resulting in an equally similar local field and SERS enhancements for both metals, as has been shown by numerical simulations.[9,47] Since we used Au and Ag NRs not only with similar size and LSPR wavelength but also with comparable quality in size uniformity and LSPR line width, potential effects derived from these factors can be excluded, which may not have been strictly observed in previous comparisons. Nevertheless, it remains challenging to ensure the same coverage degree with thiolated RaR molecules in our comparison, since the Ag−S bonding strength is generally weaker than that of Au−S bonding.[48]

Biocompatibility of SERS-encoded Ag@PMA NRs. The biocompatibility of Ag@RaR@PMA NRs was first evaluated by incubation with J774 macrophages, using all five Ag@RaR@PMA NRs, as well as CTAC-capped and PEG-capped NRs, for comparison. Particle concentrations and incubation times were maintained constant in all incubation experiments. Two cell assays were conducted in parallel using the 3-(4,5-dimethylthiazol-2-yl)2,5-diphenyl tetrazolium bromide (MTT) test and the lactate dehydrogenase (LDH) test, to measure cell viability and cytotoxicity, respectively. The MTT reagent interacts with

metabolically active cells to form a purple formazan product that can be quantified by spectrophotometry. The LDH assay relies on measuring the level of extracellular LDH released from damaged cells, which can also be spectrophotometrically quantified. For each system, the cell supernatant was transferred to a clean well for the LDH assay, leaving those cells containing Ag NRs, that were subsequently subjected to the MTT assay (Figure 4). For the highest particle
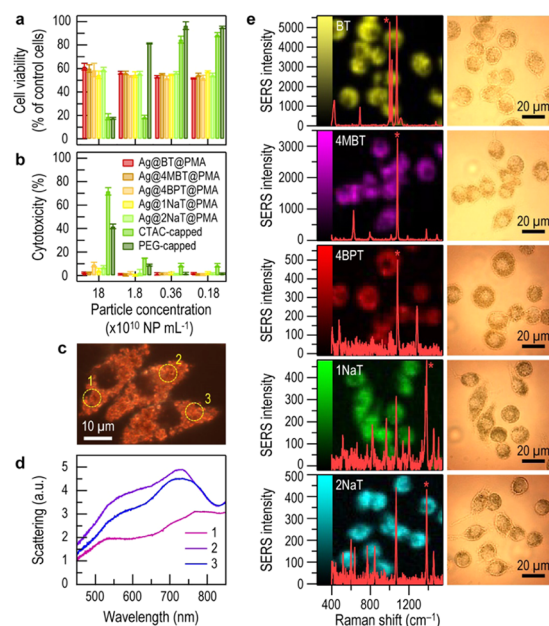

Figure 4. Cytotoxicity of Ag@RaR@PMA NRs and their application to SERS imaging of J774 macrophage cells. (a) Cell viability obtained from the MTT assay and (b) cytotoxicity obtained from the LDH assay, after 24 h of incubation with seven Ag NR samples, as labeled, at different particle concentrations. Error bars denote standard deviations resulting from triplicate experiments. (c) Real-color darkfield scattering image and (d) dark-field scattering spectra measured from three individual J774 cells containing Ag@BT@PMA NRs. (e) SERS images measured from J774 cells containing Ag@RaR@PMA NRs with overlaid SERS spectra (left), and bright-field images of the same cells (right). SERS images were collected in the streamline mode, with an integration time of 2 s, using a 785 nm laser at 6.15 mW and a 40× water immersion objective (NA = 0.8).

concentration (1.8×10^{11} NP/mL), both assays indicated that CTAC-capped and PEG-capped Ag NRs are highly cytotoxic, and a dose−response effect was observed in both assay readouts. The cytotoxicity of CTAC-capped and PEG-capped Ag NRs can be attributed to different mechanisms. CTAC itself is highly cytotoxic because of its surfactant ability to damage cell membranes,[49] resulting in widespread cell lysis (Figure S12). In contrast, cytotoxicity of PEG-capped Ag NR is likely related to Ag degradation and the toxicity of released Ag+ ions, based on the observation that NP-cellular uptake is observed without apparent cell membrane lysis, yet a low metabolic activity is detected via the MTT assay. Regarding Ag@RaR@PMA NRs, all optical observations suggest that active cellular uptake of NRs occurs to a high degree (note the uniform brown cellular staining in Figure S12a), yet the results from the MTT assay suggest a decrease in cellular metabolic activity, which is actually due to a distortion in the final absorbance readout due to this high NP-loading capacity (Figure S12b). Considering the extremely low cytotoxicity

determined from the LDH assay, we hypothesized that the corresponding cell viability was underestimated in the MTT assay. Indeed, the same observations can be made upon decreasing the NP concentration by 100-fold (Figure 4). These results suggest that the relatively low viability indicated by the MTT assay for Ag@RaR@PMA NRs is not reliable, likely due to a chemical or physical interference between the MTT reagent and Ag@RaR@PMA NRs, which are phagocytosed to very high loading efficiencies in these cells. In contrast, the LDH assay makes use of the cell supernatant and is thus more reliable, showing negligible cytotoxicity for Ag@RaR@PMA NRs, regardless of particle concentration. Although to a lesser extent, a similar disagreement was found from parallel MTT and LDH tests using MCF-7 and HeLa cells (Figure S13). Both cell lines did undergo NP endocytosis but not to the same extent as the "professional" phagocytic cell J774; hence, the interference noted in the MTT assay is less extreme. We therefore propose that the LDH assay is more reliable for evaluating cell viability in our systems and Ag@RaR@PMA NRs do not exhibit a significant cytotoxicity.

To further analyze cellular uptake, we quantitatively compared the uptake efficiency among different cell lines by inductively coupled plasma-mass spectrometry (ICP-MS), keeping the applied NR concentration and incubation conditions constant. After 24 h of incubation at 37 °C, the proportion of Ag@RaR@PMA NRs endocytosed by J774, MCF-7, and HeLa cells were $(63 \pm 15)\%$, $(5 \pm 2)\%$, and $(11 \pm 6)\%$, respectively. Apart from their different phagocytic abilities, another possible reason behind the relatively low cellular uptake by MCF-7 and HeLa cells is the negatively charged surface of Ag@RaR@PMA NRs (see ζ-potential plots for all five Ag@RaR@PMA samples in Figure S14), which is known to hamper their penetration in cells.[50,51] The negative ζ-potential originates from the carboxylic groups on the PMA surface, which provide Ag NRs with colloidal stability via electrostatic repulsions. An additional polymer coating, such as a cationic layer of poly-L-arginine hydrochloride surrounding the PMA layer, can further impart positive surface charges to the NRs (ζ-potential $+13.4 \pm 2.7$ mV), thereby enhancing the cellular uptake, as recently demonstrated for Au NPs.[42]

Application of Ag@RaR@PMA NRs in SERS Imaging of Live Cells. Ag@RaR@PMA NRs are noncytotoxic and therefore safe for intracellular applications such as SERS imaging of live cells. Ideally, intracellular Ag@RaR@PMA NRs should remain nonaggregated, with a minimum interparticle distance above 10 nm due to the PMA layer (~5 nm thick), thereby retaining the resonant condition with the 785 nm laser for SERS measurements. To verify the LSPR band of intracellular Ag@RaR@PMA NRs, we used dark-field scattering microscopy (DFM), taking Ag@BT@PMA NRs as an example.[52] Upon incubation of J774 macrophages with Ag@BT@PMA NRs, dark-field microscopy under white light illumination revealed abundant accumulation of NRs inside the J774 cells, both in the cytoplasm and in the perinuclear region (Figure 4c). The scattering spectra measured from arbitrarily selected small areas within the cells show broad LSPR bands in the NIR (Figure 4d), which should efficiently couple to the 785 nm laser used in SERS measurements. The observed band broadening, compared to the corresponding colloid, can be attributed to NR clustering within endosomes, which would confirm internalization via an endocytic pathway.[53]

Strong SERS signals were recorded from J774 cells containing different SERS nanotags (Figure 4e). Notably, the SERS signals were strong enough to enable the use of the streamline scanning mode to generate SERS maps rapidly (10 min for a single XY map of 104 μm × 104 μm, with a resolution of 1.6 μm). All SERS nanotags retained their characteristic fingerprints, as recorded when dispersed in an aqueous solution. The corresponding SERS maps were obtained by plotting the intensity of a specific vibration, namely, 1001 cm^{-1} (BT), 1081 cm^{-1} (4MBT), 1080 cm^{-1} (4BPT), 1371 cm^{-1} (1NaT), and 1382 cm^{-1} (2NaT). The contour and nuclei of individual J774 cells can be clearly distinguished in the SERS maps. We additionally performed SERS imaging under the same conditions using MCF-7 cells (Figure S15). Due to the lower uptake efficiency by this cell line, the resulting SERS signals are weaker than those observed from J774 cells. In this case, the SERS signals were found to be mostly distributed near the perinuclear region, which also supports the weaker NP uptake and clustering within endosomes. In spite of such minor differences, all SERS nanotags displayed identical fingerprints in solution and within MCF-7 cells, thereby confirming the protective effect of the PMA layer for RaR molecules in a cellular environment.

To assess the detection limit for cellular SERS imaging, we explored the effect of particle concentration on the SERS imaging performance using Ag@BT@PMA NRs, which exhibit the strongest SERS signal of all five nanotags. J774 cells were incubated with Ag@BT@PMA NRs at varying particle concentrations, ranging from 4.8×10^8 to 2.4×10^{10} NP/mL, under the same incubation conditions. After 24 h of incubation, the cell supernatants were collected and analyzed by ICP-MS. In combination with these ICP-MS measurements, correlative SERS, reflectance, and fluorescence imaging were conducted (Figure 5a−c). The use of reflectance imaging allowed us to detect the NRs themselves, whereas fluorescence imaging was employed to determine the cell viability, via a "live/dead assay", after SERS imaging. SERS imaging was conducted in the streamline mode for rapid scanning, at a laser power of 6.15 mW. The lowest intracellular particle
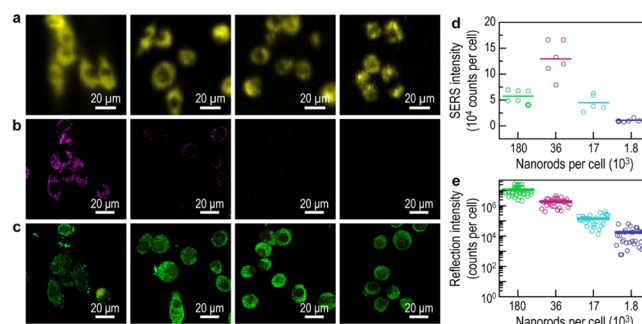

Figure 5. Effect of particle concentration on SERS signal and cell viability. (a) SERS and (b) reflection images of J774 live cells with Ag@BT@PMA NRs at different concentrations. From left to right, the intracellular particle concentrations were estimated as 1.8×10^5, 3.6×10^4, 1.7×10^4, and 1.8×10^3 NPs per cell. Each SERS map was normalized against its maximum value for clear display of the SERS images. The reflection images were recorded with identical settings and postprocessing. (c) Live/dead assay to show cell viability after SERS measurements. Live cells are shown in green and dead cells in red. (d, e) Dependence of SERS intensity (d) and reflection intensity (e) on the number of Ag NRs per cell.

concentration corresponded to 1800 NPs per cell; at this concentration, the SERS images of J774 cells become blurred due to the inherently lower signal-to-noise ratio, but the SERS maps still retained sufficient quality for analysis. As can be seen by comparing Figure 5a and b, the visual limit of detection for reflection imaging of NRs is significantly lower than that for SERS imaging. Interestingly, although the reflection intensity appears to be roughly proportional to the intracellular particle concentration, this is not always the case for SERS signals (Figure 5d,e). It should be noted that the strong scattering of light by highly concentrated NPs may hinder the excitation laser from interacting with all internalized nanotags. Additionally, the SERS signal from nanotags may also decay rapidly due to multiple scattering and absorption. SERS measurements for the sample with the highest intracellular particle concentration (1.8×10^5 NP per cell) were repeated on the following day, thereby allowing the cells to undergo an additional cycle of cell division. Assuming that NPs are also redistributed during each cell division, we should see a subsequent reduction of particle density in each cell. Indeed, we observed a change in the relationship between SERS intensity and NP concentration (Figure S16). These results suggest that there is a NP threshold concentration in cells to record the strongest SERS signal. It is worth mentioning that all cells were alive after SERS measurements (Figure 5c), again confirming the biocompatibility of Ag@PMA NRs and the negligible light-induced effects when using a low power of the 785 nm laser.

High-Power Laser Irradiation. Our discussion on intracellular applications has been so far limited to the use of low-power laser excitation (3−14 mW), where there is no significant effect from photothermal conversion, thereby avoiding a potential negative impact on cell viability and damage of RaR molecules. An example hereof is highlighted in Figure S17, which shows that exposure of J774 cells containing Ag@PMA NRs to laser irradiation at 1.8 W for 10 min results in a decrease in the SERS signal intensity and stimulation of cytotoxicity post irradiation. We therefore investigated the effect of high-power laser radiation (∼1 W) on Ag@PMA NRs, which is relevant toward potential applications in photothermal therapy, laser-induced reshaping, and other linear/nonlinear optical processes.

When irradiating Ag NP-containing cells with a NIR laser at high power, two possible effects may contribute to cell death: first is localized heating caused by photothermal effects and second is heat- or light-induced Ag degradation and leakage of toxic Ag^+ ions. The latter effect is associated with degradation in the protective ability of the PMA layer when exposed to heat, laser light, and/or the complex cell environment, individually or simultaneously, which was not fully considered in the stability tests above. We therefore designed two schemes, as illustrated in Figure 6a,b: first, J774 cells containing Ag@PMA NRs were exposed to high-power 808 nm laser irradiation, potentially combining the effects of toxic Ag^+ ions and photothermal heating; second, Ag@PMA NRs dispersed in cell media were exposed to the 808 nm laser independently and then cooled down to 37 °C and added to the J774 cell culture, thereby excluding the photothermal effect but retaining the potential cytotoxic effect of Ag^+ ions.

As can be observed in Figure 6c, significant levels of cytotoxicity were only observed when cells were irradiated with a high laser power (3.0 W/cm^2), in the presence of Ag@PMA NRs. On the contrary, when Ag@PMA NRs were irradiated separately and then added to the cell culture, no cytotoxic
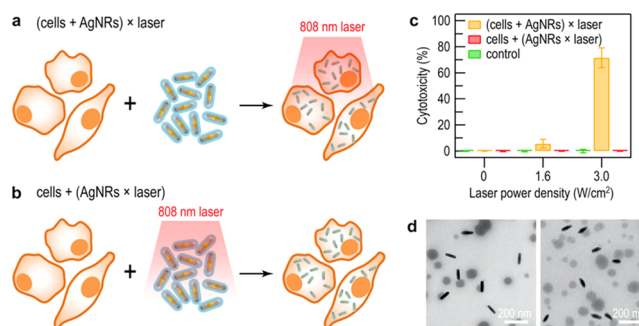

Figure 6. Effect of photothermal heating and Ag^+ release upon 808 nm laser radiation at high power. (a, b) Schematic representation of the experiments, where Ag@PMA NRs were either irradiated together with J774 cells or treated separately in complete cell media. In both cases, the exposure time was 10 min. (c) Results of the LDH cell viability assay for both schemes; error bars denote standard deviation resulting from duplicate experiments. Control samples are J774 cells not exposed to Ag@PMA NRs. (d) TEM images of AgNR@PMA NRs dispersed in complete cell media after laser radiation at 1.6 W/cm^2 (left, effective laser power 0.60 W) and at 3.0 W/cm^2 (right, effective laser power 1.12 W).

effects were observed. In other words, under high-power laser irradiation, Ag@PMA NRs remain noncytotoxic in the cell environment, but cell death may occur due to photothermal effects. Interestingly, when we investigated the effect of laser irradiation on Ag@PMA NRs themselves, reshaping was observed for NRs that were treated by a high laser power (808 nm laser at 3.0 W/cm^2) (Figure 6d). Energy-dispersive X-ray (EDX) analysis confirmed that some of the Ag NRs were sulfidized during this process (Figure S18). The source of sulfide/sulfur might be related to byproducts of proteins found in complete cell media upon laser heating.

CONCLUSIONS

In summary, we demonstrated an efficient method for the preparation of monodisperse Ag@PMA NRs with tunable optical response, outstanding long-term stability, extremely low cytotoxicity, and high biocompatibility, thereby overcoming the challenges associated with bioapplications of Ag NPs. As a result of the protective polymer (PMA) layer, Ag@PMA NRs retain their structural and optical properties against various external stimuli, including light, heat, corrosive agents, and a biological environment, with an effective suppression of the release of toxic Ag^+ ions. This method readily allows LSPR band tuning within the first biological transparency window, as well as encoding Ag NRs with different RaR molecules, thereby giving rise to biocompatible SERS nanotags with long-term stability. We additionally demonstrated intracellular SERS imaging of live cells using five different RaR molecules, with emphasis on cell viability, detection limits, photothermal effects, and the possibility of laser-induced release of Ag^+ ions. Our findings regarding stability, cytotoxicity, and SERS mapping can be readily extended to other Ag and Ag-containing NPs.

METHODS

Chemicals. Tetrachloroauric acid trihydrate (HAuCl$_4$·3H$_2$O, ≥99%), citric acid (≥99.5%), sodium borohydride (NaBH$_4$, 99%), L-ascorbic acid (≥99%), silver nitrate (AgNO$_3$, ≥99%), hexadecyl-trimethylammonium bromide (CTAB, ≥99%), hexadecyltrimethy-lammonium chloride (CTAC, 25 wt % in water), O-[2-(3-

mercaptopropionylamino)ethyl]-O'-methylpoly(ethylene glycol) (thiolated PEG, MW 5000 g/mol), benzenethiol (BT, ≥98%), 4-methylbenzenethiol (4MBT, 98%), biphenyl-4-thiol (4BPT, 97%), 1-naphthalenethiol (1NaT, 99%), 2-naphthalenethiol (2NaT, 99%), poly(isobutylene-alt-maleic anhydride) (average MW ∼ 6000 g/mol), dodecylamine (98%), 1-decanol, tetrahydrofuran (THF, 99.85%, extra dry), chloroform (CHCl$_3$, ≥99.8%), and sodium hydroxide (NaOH, >97%) were purchased from Sigma-Aldrich. Hydrochloric acid solution (37 wt %) was purchased from Fisher Chemical. All chemicals were used without further purification. Milli-Q water (resistivity 18.2 MΩ·cm at 25 °C) was used in all experiments. All glassware was washed with aqua regia, rinsed with Milli-Q water, and dried prior to use. Dulbecco's modified Eagle's medium (DMEM), fetal bovine serum (FBS), and penicillin−streptomycin (PS) were purchased from Invitrogen. FBS and PS were used at 10% and 1%, respectively, to prepare complete DMEM (cDMEM). Lactate dehydrogenase (LDH) kits were purchased from Pierce (Invitrogen). MTT kits were purchased from Roche. All cells were grown in cDMEM, and either trypsin (HeLa and MCF-7) or pipetting (J774) was used for cell passage.

Synthesis of Ag NRs. Ag NRs were prepared using Au BP-directed Ag overgrowth, modified from a previous report.[36] For the synthesis of Au BPs,[38] a freshly prepared NaBH$_4$ solution (0.025 M, 0.25 mL) was mixed with an aqueous solution composed of HAuCl$_4$ (1 mM, 2.5 mL), citric acid (0.02 M, 2.5 mL), and CTAC (0.1 M, 5 mL), under vigorous stirring. The resulting seed solution was aged in a water bath at 80 °C for 2 h under mild stirring. The as-prepared seed solution (2 mL) was injected into an aqueous growth solution containing CTAB (0.1 M, 80 mL), HAuCl$_4$ (0.01 M, 4 mL), AgNO$_3$ (0.01 M, 0.8 mL), HCl (1 M, 1.6 mL), and ascorbic acid (0.1 M, 0.64 mL) under vigorous stirring. The reaction solution was kept in a water bath at 30 °C for at least 4 h under stirring. For Ag overgrowth, the as-prepared Au BP dispersion ([Au] ∼0.5 mM, 80 mL) was centrifuged at 7000 rpm for 20 min and redispersed in CTAC (0.01 M, 40 mL), followed by subsequent addition of AgNO$_3$ (0.01 M, 8 mL) and ascorbic acid (0.1 M, 4 mL). The mixed solution was kept in a water bath at 60 °C for 2 h under stirring, to ensure Ag overgrowth. As-prepared Ag NRs were centrifuged at 6000 rpm for 20 min and redispersed in water. In the stability test (Figure 2, left), the CTAC concentration in CTAC-capped Ag NRs was estimated to be <0.05 mM. PEG-capped Ag NRs in the stability test (Figure 2, middle) were prepared by mixing CTAC-capped Ag NRs (4.5 × 10^{10} NP/mL, 1 mL) with excess thiolated-PEG (1 mM, 100 µL) at room temperature overnight. PEG-capped Ag NRs were centrifuged at 6000 rpm for 20 min and redispersed in water.

Synthesis of Au NRs. Au NRs were prepared using a modified seeded growth method, using CTAB and n-decanol as binary surfactants according to a previous report.[45] Growth solutions A (CTAB 50 mM, n-decanol 13.5 mM) and B (CTAB 50 mM, n-decanol 11 mM) were prepared by dissolving 9.111 g of CTAB together with 1.068 g and 870.5 mg of n-decanol in 500 mL of warm water, respectively. Both growth solutions were stirred at 50 °C for 1 h and then cooled down to room temperature. A typical synthesis involves three steps. First, for the synthesis of 1−2 nm Au seeds, a freshly prepared ascorbic acid solution (0.1 M, 0.025 mL) and a freshly prepared NaBH$_4$ solution (0.02 M, 0.2 mL) were successively added to a mixture composed of growth solution A (CTAB 50 mM, n-decanol 13.5 mM, 5 mL) and HAuCl$_4$ (0.05 M, 0.05 mL). The resulting seed solution was aged in a water bath at 25 °C for 30 min under mild stirring. Second, for the synthesis of small Au NRs (21 nm × 7.5 nm), the aged seed solution (0.6 mL) was injected into an aqueous solution containing growth solution A (CTAB 50 mM, n-decanol 13.5 mM, 10 mL), HAuCl$_4$ (0.05 M, 0.1 mL), AgNO$_3$ (0.01 M, 0.08 mL), HCl (1 M, 0.7 mL), and ascorbic acid (0.1 M, 0.13 mL), under vigorous stirring. The reaction mixture was kept in a water bath at 25 °C for at least 4 h under stirring. The as-prepared small Au NR solution was centrifuged at 14 000 rpm for 45 min in 2 mL tubes. The precipitate was redispersed in CTAB solution (10 mM, 10 mL) and subjected to centrifugation under the same conditions, twice. For the growth of Au NRs (33 nm × 102 nm), the small Au NR

solution (0.1 mL, OD$_{400}$ = 9) was injected into a mixture of growth solution B (CTAB 50 mM, n-decanol 11 mM, 80 mL), HAuCl$_4$ (0.05 M, 0.8 mL), AgNO$_3$ (0.01 M, 1.6 mL), HCl (1 M, 3 mL), and ascorbic acid (0.1 M, 0.64 mL), under vigorous stirring. The reaction mixture was kept in a water bath at 28 °C for at least 4 h under stirring. As-prepared Au NRs were centrifuged at 4000 rpm for 20 min twice and redispersed in water.

Preparation of the Polymer. The amphiphilic polymer, PMA, was prepared as previously reported.[31,32] Briefly, 2.7 g of dodecylamine dissolved in anhydrous THF (100 mL) was quickly injected into a round-bottom flask containing 3.085 g of poly(isobutylene-alt-maleic anhydride). The mixture was sonicated for a few seconds and then stored at 60 °C for 3 h under vigorous stirring, during which the solution gradually transformed from cloudy to transparent. The transparent mixture was concentrated to about 30 mL by rotary evaporation and then kept under reflux overnight. The solvent was then removed by rotary evaporation until the polymer was completely dry (pale-yellow solid). Finally, the resulting polymer was dissolved in chloroform (40 mL), yielding a calculated concentration of monomer units of 0.5 M. The polymer solution was sealed in a glass vial and stored in a freezer for further use.

SERS Encoding and Polymer Encapsulation. Ag and Au NRs were encoded with thiolated hydrophobic molecules (DDT, BT, 4MBT, 4BPT, 1NaT, 2NaT) and encapsulated with PMA, according to previous reports.[33,34] Briefly, CTAC-capped Ag NRs or CTAB-capped Au NRs were carefully washed to remove excess CTAC/CTAB and concentrated into an aqueous solution (1 mL) at a concentration of 8 × 10^{11} NP/mL. PEG solution (0.1 mM, 1 mL) was added dropwise to the NR colloid under stirring. The mixture was kept at room temperature for 3 h and then centrifuged to remove excess PEG and CTAC/CTAB. PEG-prestabilized NRs were stirred vigorously together with a chloroform solution of hydrophobic thiols (2.5 mM, 2 mL) for 30−60 min to complete the phase transfer. Addition of HCl (37%, 10 µL) can help promote phase transfer. Upon transfer into chloroform, the NRs were mixed with ethanol (0.5 mL) and centrifuged to remove excess of free thiols. The precipitate was redispersed in chloroform (2 mL) and mixed with a chloroform solution of PMA (0.05 M, 0.2 mL), in a 15 mL round-bottom beaker. Chloroform was then removed by rotary evaporation. The resulting solid thin films containing NRs were dissolved in NaOH solution at pH = 12. To remove empty PMA capsules and remaining NaOH, PMA-coated NRs were centrifuged and redispersed in water thrice.

Cell Viability Tests. LDH and MTT assays were used to evaluate the viability of cells after exposure to Ag NRs. Cells were seeded at 3 × 10^5 cells/mL (J774), 1 × 10^5 cells/mL (HeLa), or 5 × 10^4 cells/mL (MCF-7) in 96-well plates (100 µL/well) and allowed to adhere overnight. The following day, cell media was removed and replaced with Ag NRs diluted in cDMEM (100 µL/well). After 24 h of incubation at 37 °C, cells were washed and cell viability was tested using commercial LDH and MTT kits. In brief, for LDH measurements, 50 µL of the cell supernatant was transferred to a clean 96-well plate and 50 µL of the LDH reagent was added. Positive (10% v/v lysis buffer) and negative (10% v/v water) controls were included to determine maximum and spontaneous LDH release, respectively. After 30 min at room temperature, 50 µL of the STOP solution was added and the absorbance values at 490 and 680 nm were read. For the MTT test, the remaining 50 µL of the cell supernatant was discarded and 100 µL of the MTT reagent (1/20 in cDMEM) was added to each well. After 1 h at 37 °C, supernatants were removed and 100 µL of DMSO was added to each well. Absorbance was read at 550 nm.

ICP-MS Measurements. ICP-MS (iCAP-Q$_c$ Thermo) was used to quantify particle concentration in Ag NR colloids, as well as the level of cellular uptake. Samples of 20−200 µL were treated with a mixture of aqua regia (400 µL) and HNO$_3$ (300 µL) for 24 h and then diluted to 2 mL with water. Additional HNO$_3$ was used to minimize the formation of the AgCl precipitate. Still, we found that the Ag mass concentration could not be measured correctly in our ICP-MS system. Therefore, we calculated the particle concentration of Ag@PMA NR samples using the Au mass concentration obtained

from ICP-MS and the sizes of Au BPs measured from TEM images. For estimation of cellular uptake, cells were seeded in 48-well plates at 5×10^5 cells/mL (J774), 1×10^5 cells/mL (HeLa), or 5×10^4 cells/mL (MCF-7) in a volume of 200 μL/well. The following day, cell media was replaced with Ag NRs diluted in cDMEM (200 μL/well). After 24 h of incubation at 37 °C, cell supernatants and cells were collected separately for ICP-MS measurements. In the cases of HeLa and MCF-7, cells were detached with trypsin, counted, and frozen overnight. J774 cells, which do not respond to trypsin, were frozen in the 48-well plate, and the cell number was determined from microscopy images. The percentage of particle uptake can be obtained by considering the initial amount of Ag NRs, and the proportion was observed from cell supernatants and cells.

SERS. SERS measurements were performed with a confocal Raman microscope (Renishaw inVia Raman Reflex) equipped with a 1024 × 512 charge-coupled device (CCD) camera and 1200 grooves/mm diffraction grating, using a 785 nm laser for excitation. SERS spectra of aqueous NR colloids were collected using cylindrical glass vials (1 mL) as containers, a 10× objective (NA = 0.35), an integration time of 10 s, a laser power of either 3.43 or 13.26 mW, and 5 scans for averaging. The static mode (center of scattered wavenumber 1000 cm^{-1}) was applied for obtaining most data. The expanded scan mode was applied to obtain SERS spectra over a wide range of Raman shifts (Figure 3). SERS measurements in live cells were conducted in the streamline mode, using 35 mm glass-bottomed dishes (Ibidi), a 40× water immersion objective (NA = 0.8), an integration time of 2 s, and a laser power of either 3.10 or 6.15 mW. Each SERS map was scanned for 10 min over a selected area of 104 × 104 μm^2 with a spatial resolution of 65 × 65 pixels. To prepare the cells for SERS measurements, J774 (1.5×10^5 cells per dish) or MCF-7 (5×10^4 cells per dish) cells were seeded in 35 mm dishes. The following day, the medium was replaced with 1 mL NRs dispersed in cDMEM. After a further 24 h of incubation at 37 °C, cells were washed and fresh cDMEM was added (final volume 2 mL) and the sample was used for SERS measurements.

Laser Irradiation. To test the local heating of NPs upon exposure to 808 nm laser irradiation, a 96-well plate format was used, with the same seeding density as that used in cell viability tests. Once adhered, NPs diluted in cDMEM were added (100 μL/well) and after a further 24 h incubation period, cells were washed and media was replaced with fresh cDMEM (300 μL/well) for irradiations. A spot size of 1.2 cm and power of 1.8 or 3.4 W, corresponding to power density of 1.6 or 3.0 W/cm^2, were used to irradiate each well for 10 min. Since the well diameter in the 96-well plate is 6.9 mm, the effective laser power for photothermal conversion can be estimated as 0.60 or 1.12 W for each well. An IR camera was used to record changes in temperature during the irradiation period. Immediately after irradiation, the cell media was replaced with fresh cDMEM (100 μL/well) and the cells were incubated at 37 °C for a further 24 h prior to undertaking cell viability assays as previously described.

Characterization. TEM images were obtained on a JEOL JEM-1400PLUS TEM operating at an acceleration voltage of 120 kV. Elemental maps were performed on a JEOL JEM-2100F UHR TEM operating at an acceleration voltage of 200 kV and equipped with an Oxford INCA EDX system. Extinction spectra were measured using an Agilent 8453 UV−vis diode array spectrophotometer. ζ-potential was measured with a Z-sizer instrument (Nano ZS, Nanoseries; Malvern). Cell microscopy experiments were conducted on an LSM510 Zeiss confocal microscope for bright-field imaging and on an LSM 880 Zeiss confocal fluorescence microscope for reflection and fluorescence imaging. Dark-field scattering imaging and spectroscopy were performed with an inverted dark-field microscope (Nikon Eclipse Ti-U) equipped with a monochromator (Acton) and a color video camera (Coolprix).

ASSOCIATED CONTENT

Ⓢ Supporting Information

The Supporting Information is available free of charge at https://pubs.acs.org/doi/10.1021/acs.chemmater.0c01995.

Additional experimental results of NP preparation, stability tests, and SERS measurements; synthesis of Au BP-directed Ag NRs (AuBP@Ag) with tunable LSPR wavelength; synthesis of Ag NRs of different sizes; encapsulation of differently sized Ag NRs with PMA; photothermal effects and thermal stability (PDF)

AUTHOR INFORMATION

Corresponding Author

   Luis M. Liz-Marzán − CIC biomaGUNE, Basque Research and Technology Alliance (BRTA), 20014 Donostia-San Sebastián, Spain; Centro de Investigación Biomédica en Red de Bioingenieria, Biomateriales y Nanomedicina (CIBER-BBN), 20014 Donostia-San Sebastián, Spain; Ikerbasque, Basque Foundation for Science, 48013 Bilbao, Spain; Ⓞ orcid.org/0000-0002-6647-1353; Email: llizmarzan@cicbiomagune.es

Authors

   Xiaolu Zhuo − CIC biomaGUNE, Basque Research and Technology Alliance (BRTA), 20014 Donostia-San Sebastián, Spain

   Malou Henriksen-Lacey − CIC biomaGUNE, Basque Research and Technology Alliance (BRTA), 20014 Donostia-San Sebastián, Spain; Centro de Investigación Biomédica en Red de Bioingenieria, Biomateriales y Nanomedicina (CIBER-BBN), 20014 Donostia-San Sebastián, Spain

   Dorleta Jimenez de Aberasturi − CIC biomaGUNE, Basque Research and Technology Alliance (BRTA), 20014 Donostia-San Sebastián, Spain; Centro de Investigación Biomédica en Red de Bioingenieria, Biomateriales y Nanomedicina (CIBER-BBN), 20014 Donostia-San Sebastián, Spain; Ikerbasque, Basque Foundation for Science, 48013 Bilbao, Spain; Ⓞ orcid.org/0000-0001-5009-3557

   Ana Sánchez-Iglesias − CIC biomaGUNE, Basque Research and Technology Alliance (BRTA), 20014 Donostia-San Sebastián, Spain; Centro de Investigación Biomédica en Red de Bioingenieria, Biomateriales y Nanomedicina (CIBER-BBN), 20014 Donostia-San Sebastián, Spain

Complete contact information is available at:
https://pubs.acs.org/10.1021/acs.chemmater.0c01995

Author Contributions

X.Z., D.J.d.A., and A.S.-I. contributed to the synthesis of Ag@PMA NRs. X.Z. executed NP characterization and SERS measurements. M.H.-L. prepared cell cultures and performed cell microscopy. L.M.L.-M. conceived, coordinated, and guided the project. All authors participated in discussion of results and the preparation of the manuscript.

Notes

The authors declare no competing financial interest.

■ REFERENCES

(1) Rycenga, M.; Cobley, C. M.; Zeng, J.; Li, W. Y.; Moran, C. H.; Zhang, Q.; Qin, D.; Xia, Y. Controlling the Synthesis and Assembly of Silver Nanostructures for Plasmonic Applications. *Chem. Rev.* **2011**, *111*, 3669−3712.

(2) Gilroy, K. D.; Ruditskiy, A.; Peng, H.-C.; Qin, D.; Xia, Y. Bimetallic Nanocrystals: Syntheses, Properties, and Applications. *Chem. Rev.* **2016**, *116*, 10414−10472.

(3) Wiley, B.; Sun, Y.; Xia, Y. Synthesis of Silver Nanostructures with Controlled Shapes and Properties. *Acc. Chem. Res.* **2007**, *40*, 1067−1076.

(4) Pastoriza-Santos, I.; Liz-Marzán, L. M. N,N-Dimethylformamide as a Reaction Medium for Metal Nanoparticle Synthesis. *Adv. Funct. Mater.* **2009**, *19*, 679−688.

(5) Xia, Y.; Gilroy, K. D.; Peng, H.-C.; Xia, X. Seed-Mediated Growth of Colloidal Metal Nanocrystals. *Angew. Chem., Int. Ed.* **2017**, *56*, 60−95.

(6) Langille, M. R.; Personick, M. L.; Mirkin, C. A. Plasmon-Mediated Syntheses of Metallic Nanostructures. *Angew. Chem., Int. Ed.* **2013**, *52*, 13910−13940.

(7) Baburin, A. S.; Merzlikin, A. M.; Baryshev, A. V.; Ryzhikov, I. A.; Panfilov, Y. V.; Rodionov, I. A. Silver-Based Plasmonics: Golden Material Platform and Application Challenges. *Opt. Mater. Express* **2019**, *9*, 611−642.

(8) Jiang, R.; Chen, H.; Shao, L.; Li, Q.; Wang, J. Unraveling the Evolution and Nature of the Plasmons in (Au Core)−(Ag Shell) Nanorods. *Adv. Mater.* **2012**, *24*, OP200−OP207.

(9) Mahmoud, M. A.; El-Sayed, M. A. Different Plasmon Sensing Behavior of Silver and Gold Nanorods. *J. Phys. Chem. Lett.* **2013**, *4*, 1541−1545.

(10) Jakab, A.; Rosman, C.; Khalavka, Y.; Becker, J.; Trügler, A.; Hohenester, U.; Sönnichsen, C. Highly Sensitive Plasmonic Silver Nanorods. *ACS Nano* **2011**, *5*, 6880−6885.

(11) Zhu, X.; Zhuo, X.; Li, Q.; Yang, Z.; Wang, J. Gold Nanobipyramid-Supported Silver Nanostructures with Narrow Plasmon Linewidths and Improved Chemical Stability. *Adv. Funct. Mater.* **2016**, *26*, 341−352.

(12) Reguera, J.; Langer, J.; Jiménez de Aberasturi, D.; Liz-Marzán, L. M. Anisotropic Metal Nanoparticles for Surface Enhanced Raman Scattering. *Chem. Soc. Rev.* **2017**, *46*, 3866−3885.

(13) Izak-Nau, E.; Huk, A.; Reidy, B.; Uggerud, H.; Vadset, M.; Eiden, S.; Voetz, M.; Himly, M.; Duschl, A.; Dusinska, M.; Lynch, I. Impact of Storage Conditions and Storage Time on Silver Nanoparticles' Physicochemical Properties and Implications for Their Biological Effects. *RSC Adv.* **2015**, *5*, 84172−84185.

(14) AshaRani, P. V.; Mun, G. L. K.; Hande, M. P.; Valiyaveettil, S. Cytotoxicity and Genotoxicity of Silver Nanoparticles in Human Cells. *ACS Nano* **2009**, *3*, 279−290.

(15) Giorgio, M.; Trinei, M.; Migliaccio, E.; Pelicci, P. G. Hydrogen Peroxide: a Metabolic By-Product or a Common Mediator of Ageing Signals? *Nat. Rev. Mol. Cell Biol.* **2007**, *8*, 722−728.

(16) Olson, K. R.; Gao, Y.; Arif, F.; Arora, K.; Patel, S.; DeLeon, E. R.; Sutton, T. R.; Feelisch, M.; Cortese-Krott, M. M.; Straub, K. D. Metabolism of Hydrogen Sulfide (H_2S) and Production of Reactive Sulfur Species (RSS) by Superoxide Dismutase. *Redox Biol.* **2018**, *15*, 74−85.

(17) Stone, J. R.; Yang, S. Hydrogen Peroxide: A Signaling Messenger. *Antioxid. Redox Signaling* **2006**, *8*, 243−270.

(18) Ung, T.; Liz-Marzán, L. M.; Mulvaney, P. Controlled Method for Silica Coating of Silver Colloids. Influence of Coating on the Rate of Chemical Reactions. *Langmuir* **1998**, *14*, 3740−3748.

(19) Hanske, C.; Sanz-Ortiz, M. N.; Liz-Marzán, L. M. Silica-Coated Plasmonic Metal Nanoparticles in Action. *Adv. Mater.* **2018**, *30*, No. 1707003.

(20) Sotiriou, G. A.; Sannomiya, T.; Teleki, A.; Krumeich, F.; Vörös, J.; Pratsinis, S. E. Non-Toxic Dry-Coated Nanosilver for Plasmonic Biosensors. *Adv. Funct. Mater.* **2010**, *20*, 4250−4257.

(21) Pastoriza-Santos, I.; Koktysh, D. S.; Mamedov, A. A.; Giersig, M.; Kotov, N. A.; Liz-Marzán, L. M. One-Pot Synthesis of Ag@TiO_2 Core−Shell Nanoparticles and Their Layer-by-Layer Assembly. *Langmuir* **2000**, *16*, 2731−2735.

(22) Scarabelli, L.; Schumacher, M.; Jimenez de Aberasturi, D.; Merkl, J.-P.; Henriksen-Lacey, M.; Milagres de Oliveira, T.; Janschel, M.; Schmidtke, C.; Bals, S.; Weller, H.; Liz-Marzán, L. M. Encapsulation of Noble Metal Nanoparticles through Seeded Emulsion Polymerization as Highly Stable Plasmonic Systems. *Adv. Funct. Mater.* **2019**, *29*, No. 1809071.

(23) Choi, C. K. K.; Zhuo, X.; Chiu, Y. T. E.; Yang, H.; Wang, J.; Choi, C. H. J. Polydopamine-Based Concentric Nanoshells with Programmable Architectures and Plasmonic Properties. *Nanoscale* **2017**, *9*, 16968−16980.

(24) Zhang, Y.; Wang, L.; Tian, J.; Li, H.; Luo, Y.; Sun, X. Ag@Poly(m-phenylenediamine) Core−Shell Nanoparticles for Highly Selective, Multiplex Nucleic Acid Detection. *Langmuir* **2011**, *27*, 2170−2175.

(25) Wang, S.; Shi, G. Uniform Silver/Polypyrrole Core-Shell Nanoparticles Synthesized by Hydrothermal Reaction. *Mater. Chem. Phys.* **2007**, *102*, 255−259.

(26) Caballero-Díaz, E.; Pfeiffer, C.; Kastl, L.; Rivera-Gil, P.; Simonet, B.; Valcárcel, M.; Jiménez-Lamana, J.; Laborda, F.; Parak, W. J. The Toxicity of Silver Nanoparticles Depends on Their Uptake by Cells and Thus on Their Surface Chemistry. *Part. Part. Syst. Charact.* **2013**, *30*, 1079−1085.

(27) Durán, N.; Silveira, C. P.; Durán, M.; Martinez, D. S. T. Silver Nanoparticle Protein Corona and Toxicity: a Mini-Review. *J. Nanobiotechnol.* **2015**, *13*, No. 55.

(28) Yang, Y.; Liu, J.; Fu, Z.-W.; Qin, D. Galvanic Replacement-Free Deposition of Au on Ag for Core−Shell Nanocubes with Enhanced Chemical Stability and SERS Activity. *J. Am. Chem. Soc.* **2014**, *136*, 8153−8156.

(29) Yang, M.; Hood, Z. D.; Yang, X.; Chic, M.; Xia, Y. Facile Synthesis of Ag@Au Core-Sheath Nanowires with Greatly Improved Stability against Oxidation. *Chem. Commun.* **2017**, *53*, 1965−1968.

(30) Lenzi, E.; Jimenez de Aberasturi, D.; Liz-Marzán, L. M. Surface-Enhanced Raman Scattering Tags for Three-Dimensional Bioimaging and Biomarker Detection. *ACS Sens.* **2019**, *4*, 1126−1137.

(31) Pellegrino, T.; Manna, L.; Kudera, S.; Liedl, T.; Koktysh, D.; Rogach, A. L.; Keller, S.; Rädler, J.; Natile, G.; Parak, W. J. Hydrophobic Nanocrystals Coated with an Amphiphilic Polymer Shell: A General Route to Water Soluble Nanocrystals. *Nano Lett.* **2004**, *4*, 703−707.

(32) Lin, C.-A. J.; Sperling, R. A.; Li, J. K.; Yang, T.-Y.; Li, P.-Y.; Zanella, M.; Chang, W. H.; Parak, W. J. Design of an Amphiphilic Polymer for Nanoparticle Coating and Functionalization. *Small* **2008**, *4*, 334−341.

(33) Soliman, M. G.; Pelaz, B.; Parak, W. J.; del Pino, P. Phase Transfer and Polymer Coating Methods toward Improving the Stability of Metallic Nanoparticles for Biological Applications. *Chem. Mater.* **2015**, *27*, 990−997.

(34) Jimenez de Aberasturi, D.; Serrano-Montes, A. B.; Langer, J.; Henriksen-Lacey, M.; Parak, W. J.; Liz-Marzán, L. M. Surface Enhanced Raman Scattering Encoded Gold Nanostars for Multiplexed Cell Discrimination. *Chem. Mater.* **2016**, *28*, 6779−6790.

(35) Langer, J.; Jimenez de Aberasturi, D.; Aizpurua, J.; Alvarez-Puebla, R. A.; Auguié, B.; Baumberg, J. J.; Bazan, G. C.; Bell, S. E. J.; Boisen, A.; Brolo, A. G.; Choo, J.; Cialla-May, D.; Deckert, V.; Fabris, L.; Faulds, K.; García de Abajo, F. J.; Goodacre, R.; Graham, D.; Haes, A. J.; Haynes, C. L.; Huck, C.; Itoh, T.; Käll, M.; Kneipp, J.; Kotov, N. A.; Kuang, H.; Le Ru, E. C.; Lee, H. K.; Li, J.-F.; Ling, X. Y.; Maier, S. A.; Mayerhöfer, T.; Moskovits, M.; Murakoshi, K.; Nam, J.-M.; Nie, S.; Ozaki, Y.; Pastoriza-Santos, I.; Perez-Juste, J.; Popp, J.; Pucci, A.; Reich, S.; Ren, B.; Schatz, G. C.; Shegai, T.; Schlücker, S.; Tay, L.-L.; Thomas, K. G.; Tian, Z.-Q.; Van Duyne, R. P.; Vo-Dinh, T.; Wang, Y.; Willets, K. A.; Xu, C.; Xu, H.; Xu, Y.; Yamamoto, Y. S.; Zhao, B.; Liz-Marzán, L. M. Present and Future of Surface-Enhanced Raman Scattering. *ACS Nano* **2020**, *14*, 28−117.

(36) Zhuo, X.; Zhu, X.; Li, Q.; Yang, Z.; Wang, J. Gold Nanobipyramid-Directed Growth of Length-Variable Silver Nanorods

with Multipolar Plasmon Resonances. *ACS Nano* **2015**, *9*, 7523−7535.

(37) Gómez-Graña, S.; Goris, B.; Altantzis, T.; Fernández-López, C.; Carbó-Argibay, E.; Guerrero-Martínez, A.; Almora-Barrios, N.; López, N.; Pastoriza-Santos, I.; Pérez-Juste, J.; Bals, S.; Van Tendeloo, G.; Liz-Marzán, L. M. Au@Ag Nanoparticles: Halides Stabilize {100} Facets. *J. Phys. Chem. Lett.* **2013**, *4*, 2209−2216.

(38) Sánchez-Iglesias, A.; Winckelmans, N.; Altantzis, T.; Bals, S.; Grzelczak, M.; Liz-Marza'n, L. M. High-Yield Seeded Growth of Monodisperse Pentatwinned Gold Nanoparticles through Thermally Induced Seed Twinning. *J. Am. Chem. Soc.* **2017**, *139*, 107−110.

(39) Xi, M.; Reinhard, B. M. Evolution of Near- and Far-Field Optical Properties of Au Bipyramids upon Epitaxial Deposition of Ag. *Nanoscale* **2020**, *12*, 5402−5411.

(40) Mayer, M.; Scarabelli, L.; March, K.; Altantzis, T.; Tebbe, M.; Kociak, M.; Bals, S.; García de Abajo, F. J.; Fery, A.; Liz-Marzán, L. M. Controlled Living Nanowire Growth: Precise Control Over the Morphology and Optical Properties of AgAuAg Bimetallic Nanowires. *Nano Lett.* **2015**, *15*, 5427−5437.

(41) Serrano-Montes, A. B.; Jimenez de Aberasturi, D.; Langer, J.; Giner-Casares, J. J.; Scarabelli, L.; Herrero, A.; Liz-Marzán, L. M. A General Method for Solvent Exchange of Plasmonic Nanoparticles and Self-Assembly into SERS-Active Monolayers. *Langmuir* **2015**, *31*, 9205−9213.

(42) Jimenez de Aberasturi, D.; Henriksen-Lacey, M.; Litti, L.; Langer, J.; Liz-Marzán, L. M. Using SERS Tags to Image the Three-Dimensional Structure of Complex Cell Models. *Adv. Funct. Mater.* **2020**, *30*, No. 1909655.

(43) Tanner, E. E. L.; Tschulik, K.; Tahany, R.; Jurkschat, K.; Batchelor-McAuley, C.; Compton, R. G. Nanoparticle Capping Agent Dynamics and Electron Transfer: Polymer-Gated Oxidation of Silver Nanoparticles. *J. Phys. Chem. C* **2015**, *119*, 18808−18815.

(44) Carril, M.; Padro, D.; del Pino, P.; Carrillo-Carrion, C.; Gallego, M.; Parak, W. J. In Situ Detection of the Protein Corona in Complex Environments. *Nat. Commun.* **2017**, *8*, No. 1542.

(45) González-Rubio, G.; Kumar, V.; Llombart, P.; Díaz-Núñez, P.; Bladt, E.; Altantzis, T.; Bals, S.; Peña-Rodríguez, O.; Noya, E. G.; MacDowell, L. G.; Guerrero-Martínez, A.; Liz-Marzán, L. M. Disconnecting Symmetry Breaking from Seeded Growth for the Reproducible Synthesis of High Quality Gold Nanorods. *ACS Nano* **2019**, *13*, 4424−4435.

(46) Nima, Z. A.; Davletshin, Y. R.; Watanabe, F.; Alghazali, K. M.; Kumaradas, J. C.; Biris, A. S. Bimetallic Gold Core−Silver Shell Nanorod Performance for Surface Enhanced Raman Spectroscopy. *RSC Adv.* **2017**, *7*, 53164−53171.

(47) Li, N.; Yin, H.; Zhuo, X.; Yang, B.; Zhu, X.-M.; Wang, J. Infrared-Responsive Colloidal Silver Nanorods for Surface-Enhanced Infrared Absorption. *Adv. Opt. Mater.* **2018**, *6*, No. 1800436.

(48) Pakiari, A. H.; Jamshidi, Z. Nature and Strength of M−S Bonds (M = Au, Ag, and Cu) in Binary Alloy Gold Clusters. *J. Phys. Chem. A* **2010**, *114*, 9212−9221.

(49) Alonso, L.; Cardoso, E. J. S.; Gomes, R. S.; Mendanha, S. A.; Dorta, M. L.; Alonso, A. Antileishmanial and Cytotoxic Activities of Ionic Surfactants Compared to Those of Miltefosine. *Colloids Surf., B* **2019**, *183*, No. 110421.

(50) Jiang, Y.; Huo, S.; Mizuhara, T.; Das, R.; Lee, Y.-W.; Hou, S.; Moyano, D. F.; Duncan, B.; Liang, X.-J.; Rotello, V. M. The Interplay of Size and Surface Functionality on the Cellular Uptake of Sub-10 nm Gold Nanoparticles. *ACS Nano* **2015**, *9*, 9986−9993.

(51) Mosquera, J.; Henriksen-Lacey, M.; García, I.; Martínez-Calvo, M.; Rodríguez, J.; Mascareñas, J. L.; Liz-Marzán, L. M. Cellular Uptake of Gold Nanoparticles Triggered by Host−Guest Interactions. *J. Am. Chem. Soc.* **2018**, *140*, 4469−4472.

(52) Wang, S.-H.; Lee, C.-W.; Chiou, A.; Wei, P.-K. Size-Dependent Endocytosis of Gold Nanoparticles Studied by Three-Dimensional Mapping of Plasmonic Scattering Images. *J. Nanobiotechnol.* **2010**, *8*, No. 33.

(53) Liu, M.; Li, Q.; Liang, L.; Li, J.; Wang, K.; Li, J.; Lv, M.; Chen, N.; Song, H.; Lee, J.; Shi, J.; Wang, L.; Lal, R.; Fan, C. Real-Time Visualization of Clustering and Intracellular Transport of Gold Nanoparticles by Correlative Imaging. *Nat. Commun.* **2017**, *8*, No. 15646.